Environmental Science and Pollution Research (2023) 30:53548–53565
https://doi.org/10.1007/s11356-023-26000-w

RESEARCH ARTICLE

Mesoporous Ag-functionalized magnetic activated carbon-based agro-waste for efficient removal of Pb(II), Cd(II), and microorganisms from wastewater

Omnia I. Ali[1] · Eman R. Zaki[2] · Mohga S. Abdalla[1] · Saber M. Ahmed[2]

Received: 21 July 2022 / Accepted: 14 February 2023 / Published online: 2 March 2023

Abstract
Herein, eco-friendly mesoporous magnetic activated carbon-based agro-waste nanosorbents incorporating antimicrobial silver nanoparticles (Mag@AC1-Ag and Mag@AC1-Ag) have been prepared. Various techniques (XRD, SEM/EDX, TEM, FTIR, and BET analysis) were employed to characterize the prepared nanosorbents before being utilized as novel nanosorbents to remove Pb^{+2} and Cd^{+2} ions. Mag@AC1-Ag and Mag@AC1-Ag exhibited rapid and excellent uptake of Pb^{+2} and Cd^{+2}. The pseudo-second-order kinetics and the Langmuir isotherm are more suitable for the explanation of the experimental results. The thermodynamic parameters showed that the Pb^{+2} and Cd^{+2} sorption by the nanosorbents was a spontaneous and endothermic reaction. The prepared nanosorbents can be effectively regenerated using HCl and recycled up to the fifth cycle. These nanosorbents' potential uses for eliminating Pb^{+2} and Cd^{+2} from real water samples were evaluated. Moreover, the results revealed that both Mag@AC1-Ag and Mag@AC2-Ag exhibited high antimicrobial activity against fecal coliform (gram-negative) and *Bacillus subtilis* (gram-positive).

Keywords Agro-waste · Activated carbon · Magnetite · Ag nanoparticles · Heavy metals · Removal · Antimicrobial activity

Introduction

Water is a vital necessity for survival, and providing pure water to human beings is one of the prospective development goals to be achieved up to 2030. Rapid industrial and urban growth has contributed to the generation of huge quantities of municipal and industrial wastewater that are contaminated with diverse toxic metals, organic substances, and pathogenic microorganisms. Water pollution caused by industrial, agricultural, and municipal activities has become a serious threat to human and ecosystem environments (Patel 2020; Zhang et al. 2016). Effluents discharged from industrial wastewater contain high concentrations of heavy metals (Thilakan et al. 2022), causing a serious threat to aquatic ecosystems and health problems as they are not biodegradable, toxic in nature, carcinogenic, and can accumulate in the food chain (Li et al. 2019; Wang et al. 2020). Among these metals, cadmium is discharged into the environment as a consequence of cadmium electroplating, phosphate fertilizers, Ni–Cd battery manufacture, cement manufacture, and steel production (Jain et al. 2018). It causes a number of irregularities in humans, including renal degradation, muscular cramps, proteinuria, pulmonary problems, and testicular atrophy (Zaini et al. 2009; Asuquo et al. 2017). Lead is another heavy metal that enters the environment as a result of metal corrosion, fabrications, batteries, gasoline, paints, and pigments (Bahadır et al. 2014). It accumulates in human and animal tissues and causes damage to the brain, kidney, liver, reproductive, and nervous systems and may cause severe health issues, such as abortion, sterility, neonatal deaths, and stillbirths (Parlayıcı and Pehlivan 2017). It interferes with the metabolism of vitamin D and calcium, affects the formation of hemoglobin, and causes anemia (Khajeh 2011). Based on the Environmental Protection Agency, the maximum concentration of cadmium is 0.005 mg L^{-1} and that of lead is 0.015 mg L^{-1} in drinking water (Abatal et al.

Responsible Editor: Tito Roberto Cadaval Jr

✉ Omnia I. Ali
omniaali@science.helwan.edu.eg;
omniaibrahim95@gmail.com

[1] Chemistry Department, Faculty of Science, Helwan University, Cairo 11795, Egypt

[2] Soil, Water and Environment Research Institute, Agriculture Research Centre, Giza, Egypt

2021). Therefore, at even trace concentrations, they have chronic consequences for human beings and plants.

Various technologies have been developed to remove heavy metals from wastewater. Among these technologies, adsorption is quite promising because of its high effectiveness, easy handling, the availability of various sorbent materials, and cost effectiveness (Mia et al. 2017). Activated carbon is a potent adsorbent that is employed to remove dangerous metals because of its large surface area, complex porous structure, high catalytic activity, and the presence of a wide spectrum of functional groups on its surface (Furlan and Melcer 2014). Activated carbon provides a high capacity for adsorption, a high level of surface reactivity, and a powerful affinity for contaminants at even low concentrations. In recent decades, agricultural by-products, including cotton stalk (El Zayat and Smith 2013; Akperov and Akperov 2019), sugarcane bagasse (Mohamed et al. 2015), banana peels (Zhou et al. 2017), rice straw (Zhang et al. 2018), palm shell (Issabayeva et al. 2006; Baby et al. 2019), coconut shell (Chandana et al. 2020), strawberry seeds and pistachio shells (Blachnio et al. 2020), and cotton seed shell (Uçar and Armağan 2012) have been applied as precursors to prepare various activated carbon adsorbents.

Palm shell (also known as endocarp) is a low-cost and widely available agricultural by-product in Egypt. It has been effectively converted into a well-developed activated carbon (Adinata et al. 2007; Yuliusman et al. 2017). Palm shell contains cellulose (26.6%) and hemicelluloses (27.7%), which is suitable to be employed as activated carbon to remove various pollutants (Wong et al. 2016; Baby et al. 2019; Kyi et al. 2020). Although activated carbons show maximum adsorption capacity for heavy metal removal, their use on a large scale is limited because it is notoriously difficult to separate from the solution. Iron oxide nanoparticles are great adsorbents as they have outstanding magnetic characteristics, good reusability, great biocompatibility, and a comparatively low cost (Dave and Chopda 2014; Geneti et al. 2022). A combination of activated carbon and iron oxide nanoparticles (e.g., magnetite and γ-Fe_2O_3) has been widely used to synthesize magnetic nanocomposites for easy separation and recovery (Zhang et al. 2018; Fatimah et al. 2021).

Water can be contaminated by numerous organisms, including viruses, bacteria, protozoa, and helminths (Jalali et al. 2017). Waterborne diseases are a global health threat, leading to mortality, and the high cost of their prevention and treatment make it essential to treat wastewater before disposal. Different disinfection techniques can be used to kill pathogens, but unfortunately, the conventional methods, such as chlorination, ultraviolet treatment, and ozonation, have their limitations. For example, chemical disinfectants can react with a number of the natural water constituents, developing disinfection by-products (DBPs) (Mezgebe et al. 2020), many of which are carcinogens (Furlan et al. 2017). The use of antimicrobial nanomaterials can be linked to broad-spectrum activity and is not expected to form harmful DBPs. Among these materials, Ag-based nanoparticles (AgNPs) have strong antimicrobial activity, low toxicity to humans, and no negative effects on the soil community (Najafpoor et al. 2020). As known, the silver nanoparticles' agglomeration may weaken their ability to disinfect. To control this, silver nanoparticles are incorporated into an adsorbent host matrix, providing high dispersion and preventing the aggregation of incorporated silver nanoparticles. Activated carbon can represent the most hopeful hosting material since it is an effective adsorbent for the removal of a number of contaminants (Furlan et al. 2017). The combination of Ag nanoparticles with magnetic activated carbon permits the antimicrobial materials to be regenerated easily and reused for the preceding cycles of water disinfection, limiting environmental impacts and conserving materials.

In this study, different antimicrobial activated carbon-based agro-waste nanosorbents incorporating magnetite and silver nanoparticles (AgNPs) have been prepared. Activated carbon was prepared from palm shell using two different routes of chemical activation. For the preparation of these bifunctional nanosorbents, magnetite nanoparticles were first immobilized on the prepared activated carbon samples to impart magnetic properties to them. Moreover, to add the biocidal properties to the magnetic activated carbon, AgNPs were integrated onto the previous intermediate products. This study covered the nanosorbents' preparation, characterization, and batch-mode experiments, which were performed to remove Pb^{+2} and Cd^{+2} from water and wastewater. The kinetics, equilibrium, thermodynamics, and reusability were also explored. Furthermore, the antimicrobial efficacy of the prepared nanosorbents for water disinfection was evaluated.

Experimental

Materials

Palm shell was provided by the Faculty of Agriculture, Cairo University, Egypt. KOH, NaOH, and $FeSO_4 \cdot 7H_2O$ were obtained from the Central Drug House (P) Ltd., India. K_2CO_3 and $FeCl_3$ were purchased from Qualikems Fine Chem. Pvt. Ltd., India. $Pb(NO_3)_2$ and $CdCl_2$ were purchased from LOBA Chemie, India. $AgNO_3$, fecal coliform, and *Bacillus subtilis* strains were kindly provided by the Soils, Water, and Environmental Res. Inst. (ARC) in Giza, Egypt.

Preparation of nanosorbents

Preparation of activated carbon from palm shell

Palm shell (PS) was washed, dried, and crushed using a steel mill into a fine powder. Six grams of the crushed powder were blended with a KOH or K_2CO_3 solution (20 mL, 30%, w/v). The mixture was left overnight in the oven at 120 °C before being transferred to the muffle furnace at 500 °C for 2 h. To remove the residual alkalis, the produced activated carbon (AC) was washed thoroughly with HCl (0.1 mol L^{-1}), hot, and cold distilled water until neutral pH. After all, the samples were dried at 105 °C overnight. ACs that were activated chemically with KOH and K_2CO_3 were denoted as AC1 and AC2, respectively.

Preparation of magnetite/activated carbon nanosorbents and mesoporous magnetite nanoparticles

The mesoporous magnetite/activated carbon nanosorbents were prepared as reported by Jain et al. (2018). One gram of AC was distributed in a 200 mL solution comprising $FeCl_3 \cdot 6H_2O$ (3.9 g) and $FeSO_4 \cdot 7H_2O$ (1.9 g) by vigorous stirring at 60 °C. This solution was dispersed by periodic probe sonication for 10 min. For the precipitation of the hydrated iron oxide, NaOH (10.0 mol L^{-1}) solution was added dropwise into the prepared suspension, while vigorous stirring was carried out at 60 °C until the pH reached 10–11. The suspension was then aged for 24 h at room temperature after being stirred for 2 more hours at 60 °C. Then, the formed nanosorbents (Mag@AC1 and Mag@AC2) were separated using a magnet and repeatedly rinsed with distilled water until the pH was neutral. Furthermore, similar to the procedures described above but without the addition of AC, magnetite nanoparticles were synthesized.

Synthesis of Mag@AC1-Ag and Mag@AC2-Ag

Practically, the AgNPs synthesis was based on the traditional reduction approach of Lee and Meisel (1982). In brief, 250 mL of $AgNO_3$ solution (0.005 mol L^{-1}) was heated until it started to boil. Then, 10 mL of sodium citrate (1%) was added, and the mixture was heated until it became pale yellow. The mixture was left undisturbed while it cooled to room temperature. Then this solution was poured into the beaker containing the Mag@AC1 or Mag@AC2, and the mixture was vigorously stirred at 60 °C for 4 h using a magnetic stirrer. After that, the mixture was left undisturbed for 24 h at room temperature. Magnetite/activated carbon/silver (Mag@AC1-Ag and Mag@AC2-Ag) nanosorbents were separated by a magnet. The separated samples were then dried at 80 °C for 6 h. The prepared nanosorbents were grinded and kept for future use in sealed plastic containers.

Characterization of magnetite, Mag@AC1-Ag, and Mag@AC2-Ag nanosorbents

X-ray diffractometer (Bruker D8 Advance, Germany) was used to obtain X-ray diffraction data of the prepared nanosorbents over a 2θ range of 10–80° and Cu target (1.5406 Å). The nanosorbents' surface morphology was described employing a scanning electron microscope (SEM Quanta FEG 250 with field emission gun, FEl Company, the Netherlands). The nanosorbents' particle size was estimated using a high-resolution transmission electron microscope (model JEM-2100HRT, Japan) that operated at 200 kV. A Fourier-transform infrared (FTIR-6100 Jasco, Japan) spectrometer was utilized for recording the FT-IR spectra of the prepared nanosorbents in the range of 4000–400 cm^{-1} with a spectral resolution of 4 cm^{-1} at room temperature. The BET surface area and pore structure of the nanosorbents were evaluated with a Quantachrome surface area analyzer (model Autosorb-1) in an N_2 atmosphere at 77 K using the BJH method from the desorption data. In order to get rid of moisture, the prepared nanosorbents were degassed at 200 °C for 24 h prior to measurement.

Sorption studies

To explore the removal of Pb^{+2} and Cd^{+2} ions, batch experiments were conducted by shaking the solution of each ion (25 mL) with 0.05 g of the nanosorbent in a rotary shaker with a 180-rpm agitation speed at 25 °C. In addition, to optimize the experimental conditions for the removal of each ion, several parameters, including the initial pH (2–7), contact time (10–180 min), mass of nanosorbent (0.01–0.2 g), initial Pb^{+2} or Cd^{+2} concentration (5–400 mg L^{-1}), and temperature (25, 35, 45, and 55 °C) were investigated. After reaching equilibrium, the nanosorbents were detached using a strong magnet, and the supernatant was separated using a 0.20-µm syringe filter.

The metal ions' remaining concentration was determined using atomic absorption spectroscopy (240AAFS, Agilent, USA). The removal efficiency % of Pb^{+2} or Cd^{+2} was estimated using Eq. (1):

$$\text{Removal efficiency } \% = \frac{\left(C_i - C_e\right)}{C_i} \times 100 \quad (1)$$

where C_i and C_e are the initial and equilibrium Pb^{+2} or Cd^{+2}concentrations, respectively, in the solution (mg L^{-1}).

The sorption capacity (q_e) of the prepared nanosorbents for Pb^{+2} and Cd^{+2} was estimated using Eq. (2):

$$q_e(\text{mg g}^{-1}) = \frac{(C_i - C_e)\ V}{m} \tag{2}$$

where the solution volume (L) is V and the nanosorbent mass (g) is m.

Sorption kinetics

The sorption kinetics are important for describing the sorption mechanisms and rates, and it relies upon the chemical and physical features of the sorbent. For describing the sorption kinetics, Lagergren pseudo-first-order, pseudo-second-order, and intra-particle diffusion models were applied.

Lagergren pseudo-first-order model presumes that one metal ion is sorbed onto one sorption site on the sorbent surface. The equation of the Lagergren pseudo-first-order model is defined as:

$$ln(q_e - q_t) = ln\ q_e - k_1 t \tag{3}$$

where q_e and q_t (mg g^{-1}) are the sorption capacities for Pb^{+2} and Cd^{+2} at equilibrium and time t (min), respectively, and k_1 (min^{-1}) is the pseudo-first-order rate constant.

On the other hand, the pseudo-second-order kinetics presumes that one metal ion is sorbed onto two sorption sites on the sorbent surface. The pseudo-second-order kinetic model is presented as:

$$\frac{t}{q_t} = \frac{1}{k_2 q_e^2} + \frac{t}{q_e} \tag{4}$$

where k_2 is the pseudo-second-order rate constant (g mg^{-1} min^{-1}).

5The Weber-Morris equation can be used to express the intra-particle diffusion model, which can be expressed as follows:

$$q_t = k_d\ t^{0.5} + C \tag{5}$$

where k_d is the intra-particle diffusion rate constant (mg g^{-1} $min^{-1/2}$) and C is the width of the boundary layer.

In addition, the Boyd model (Pholosi et al. 2020) is employed to discriminate between film and intra-particle diffusion to determine the genuinely rate-controlling step using Eq. (6) as follows:

$$G = \frac{q_t}{q_e} = 1 - \frac{6}{\pi^2} \exp(-B_t) \tag{6}$$

Rearranging Eq. (6):

$$B_t = -0.4977 - ln\left(1 - \frac{q_t}{q_e}\right) \tag{7}$$

where G denotes the fraction of Pb^{+2} or Cd^{+2} sorbed at time t and the mathematical function of G is B_t. The estimated B_t values using Eq. (7) were plotted against t.

Sorption isotherms

Sorption isotherms illustrate the mathematical correlation between the sorbate quantity and the sorbate concentration at equilibrium that still present in the solution at a fixed temperature. The equilibrium sorption data has been explored using Langmuir, Freundlich, Dubinin–Radushkevich, and Temkin isotherms (Abatal et al. 2021).

The Langmuir isotherm linearized form can be represented by:

$$\frac{C_e}{q_e} = \frac{1}{K_L q_{max}} + \frac{C_e}{q_{max}} \tag{8}$$

where q_{max} (mg g^{-1}) is the maximum Langmuir sorption capacity and the Langmuir constant is K_L (L mg^{-1}), which is related to binding site affinity and sorption bonding energy.

Freundlich isotherm is represented by:

$$log\ q_e = \frac{1}{n} log\ C_e + log\ K_F \tag{9}$$

where the Freundlich constant is K_F (mg g^{-1}), which represents sorption capacity, and n (L mg^{-1}) is the sorption intensity.

Dubinin–Radushkevich isotherm (D-R) model can be expressed by:

$$lnq_e = lnK_{D-R} - \beta\varepsilon^2 \tag{10}$$

where $K_{D\text{-}R}$ (mg g^{-1}) is the D-R constant and ε (mol^2 J^{-2}) is the Polanyi potential, which is equal to:

$$\varepsilon = RT\ ln\left(1 + \frac{1}{C_e}\right) \tag{11}$$

where the ideal gas constant is R (J K^{-1} mol^{-1}), and the absolute temperature is T (K). The mean sorption free energy, E (kJ mol^{-1}), is associated with the constant β and is represented by:

$$E = 1/\sqrt{2\beta} \tag{12}$$

The Temkin isotherm's linearized form is represented as follows:

$$q_e = RT/b_T\ ln\ A_T + RT/b_T\ ln\ C_e \tag{13}$$

where A_T is a constant equivalent to the maximum binding energy (L g^{-1}) and b_T (J mol^{-1}) is the Temkin isotherm constant associated with sorption heat.

Thermodynamics studies

The impact of temperature on the Pb^{2+} and Cd^{2+} sorption using magnetite, Mag@AC1-Ag, and Mag@AC2-Ag nanosorbents was investigated by performing experiments using 100 and 50 mg L^{-1} of initial Pb^{+2} and Cd^{+2} concentrations, respectively, at 298, 308, 318, and 328 K. The thermodynamic parameters, Gibbs free energy change (ΔG), enthalpy change (ΔH), and entropy change (ΔS), were evaluated using the following equations:

$$\Delta G = \Delta H - T\Delta S \tag{14}$$

$$K_d = \frac{q_e}{C_e} \tag{15}$$

$$ln\ K_d = \frac{\Delta S}{R} - \frac{\Delta H}{RT} \tag{16}$$

Regeneration and reusability studies

The probability of regeneration and reuse of sorbents is of environmental and economic concerns. For regeneration experiments, Pb- or Cd-loaded nanosorbent was first rinsed with distilled water several times to remove any metal ions that were not firmly attached to their surface. The desorption procedure was carried out by mixing 0.05 g of Pb- and Cd-loaded nanosorbents with 10 mL of HCl (0.1 mol L^{-1}) for an hour on a rotary shaker at an agitation speed of 180 rpm at 25 °C. Desorption efficiency was estimated by Eq. (17):

$$\text{Desorption efficiency } \% = \frac{\text{Amount of released metal ion}}{\text{Amount of sorbed metal ion}} \times 100 \tag{17}$$

For the reusability process, the regenerated nanosorbents were tested by following the sorption–desorption procedure for several cycles for both Pb^{+2} and Cd^{+2} removal.

Nanosorbents' antimicrobial activity

The antimicrobial activity of nanosorbents against pathogenic bacteria, including fecal coliform (gram-negative) and *Bacillus subtilis* (gram-positive), was tested utilizing the agar well diffusion method. On a nutrient agar medium, bacteria pure cultures were subcultured. Each strain was swabbed with sterile cotton swabs onto plates. A paper disc comprising the nanosorbent solution was then placed on the agar surface. After leaving the Petri dishes for 24 h at 37 °C, the width of the inhibition zone surrounding each disc was evaluated.

Results and discussion

Characterization

Point of zero charge (pH_{pzc})

The pH_{pzc} of the prepared nanosorbents was estimated using the batch equilibrium method (Jain et al. 2018). The initial pH (pH_i) of 50 mL of NaCl solutions (0.01 mol L^{-1}) was set between 2 and 12 with HCl or NaOH (0.1 mol L^{-1}) where 0.1 g of magnetite, Mag@AC1-Ag, or Mag@AC2-Ag was added. The flasks containing nanosorbents were agitated for 48 h, and the final pH (pH_f) of the solution was estimated. The difference between the pH_i and pH_f was plotted versus the pH_i. pH_{pzc} is the value obtained at the point where the resultant curve intersects the abscissa axis, with ΔpH equals 0. The obtained pH_{pzc} values of magnetite, Mag@AC1-Ag, and Mag@AC2-Ag (Fig. 1) were found to be 5.6, 6.4, and 6.0, respectively.

X-ray diffraction (XRD)

The XRD patterns of magnetite, Mag@AC1-Ag, and Mag@AC2-Ag are shown in Fig. 2a. The typical peak at 35.65° present in all three samples is attributed to the crystalline plane with a Miller index of (3 1 1), which proves the inverse spinal structure of magnetite (Bastami and Entezari 2012). The characteristic diffraction peaks at 2θ of 30.27°, 43.33°, 53.77°, 57.32°, 62.95°, 67.26°,

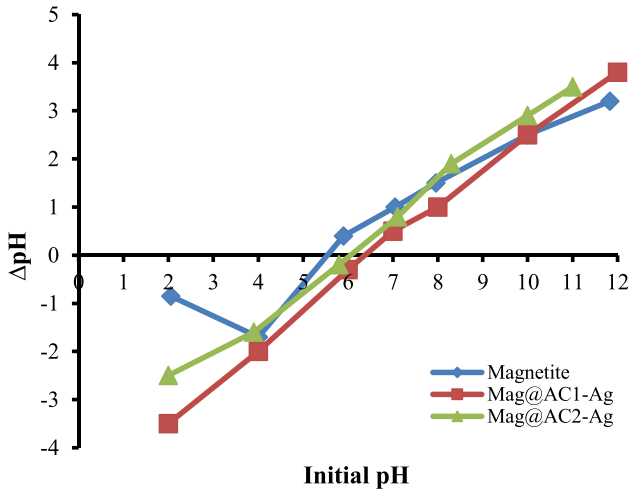

Fig. 1 pH_{zpc} for magnetite, Mag@AC1-Ag, and Mag@AC2-Ag

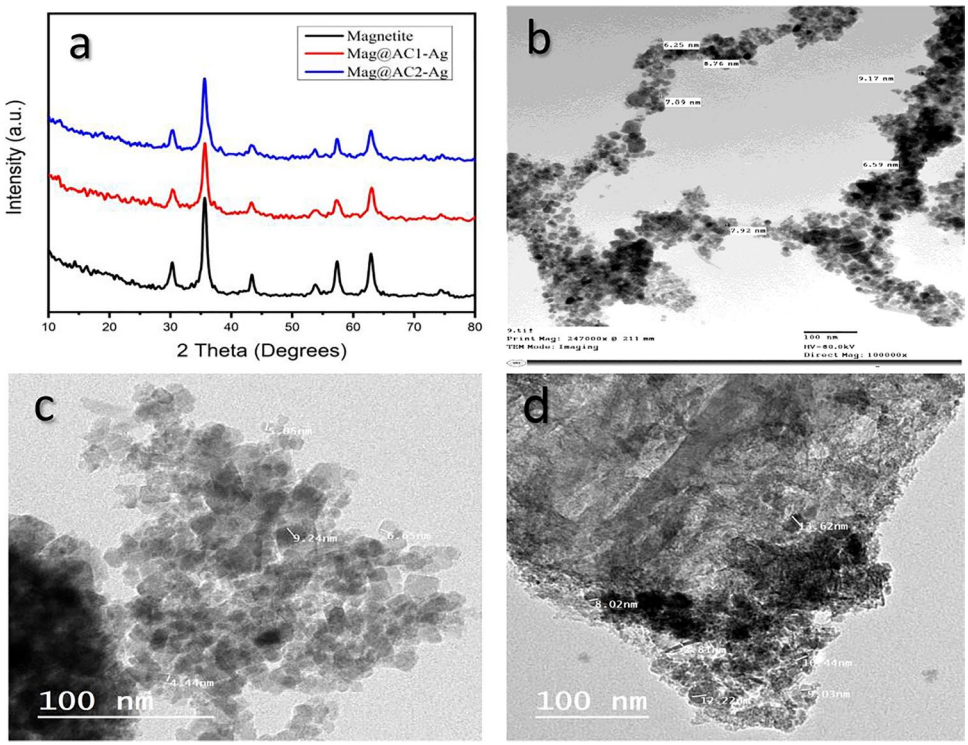

Fig. 2 XRD patterns of magnetite, Mag@AC1-Ag, and Mag@AC2-Ag (**a**) and TEM images of magnetite (**b**), Mag@AC1-Ag (**c**), and Mag@AC2-Ag (**d**)

71.43°, and 74.50° are indexed to (2 2 0), (4 0 0), (4 2 2), (5 1 1), (4 4 0), (4 4 2), (6 2 0), and (5 3 3) planes, respectively, suggesting the presence of a cubic magnetite phase (JCPDS Card no. 79–0417). In the case of Mag@AC1-Ag and Mag@AC2-Ag samples, the characteristic peaks of magnetite are still present but with less intensity, demonstrating the successful incorporation of magnetite within the activated carbon matrix. Also, weak characteristic peaks of AgNPs were presented at 2θ of 38.17°, 44.53°, and 64.44° indexed to (1 1 1), (2 0 0), and (2 2 0), planes, respectively, and this may be due to the low content of Ag nanoparticles. The XRD results for Mag@AC1-Ag and Mag@AC2-Ag samples confirm that magnetite and Ag nanoparticles have been successfully incorporated into the activated carbon matrix. The estimated crystallite size was 11.83 nm for magnetite, 13.51 nm for Mag@AC1-Ag, and 10.54 nm for Mag@AC2-Ag, all obtained using Scherrer's formula (Cullity 1956).

Transmission electron microscopy (TEM)

Figure 2b–c displays the TEM images for magnetite, Mag@AC1-Ag, and Mag@AC2-Ag samples. The figure indicates that the nanosorbents have a pseudo-spherical shape. Moreover, the figure shows that the particle sizes of magnetite, Mag@AC1-Ag, and Mag@AC2-Ag nanosorbents were in the range of 6–10, 4–10, and 8–14 nm, respectively.

Scanning electron microscopy (SEM)/energy dispersive X-ray spectroscopy (EDX)

SEM images and EDX survey are important for describing the surface morphology, physical properties, and structure of the sorbents. Figure 3 shows SEM images and EDX spectra of the prepared magnetite, Mag@AC1-Ag, and Mag@AC2-Ag nanosorbents. As revealed from the images, the magnetite nanoparticles (Fig. 3a) are agglomerated, stuck to each other, and have a spongy-like texture. Figure 3c, e shows that both Mag@AC1-Ag and Mag@AC2-Ag have porous, rough, and coarse surfaces. It can also be observed that the surfaces of both Mag@AC1-Ag and Mag@AC2-Ag samples are shiny and bright due to the precipitation of silver nanoparticles. The EDX elemental analysis shown in Fig. 3b, d, f displays major peaks of C, O, Fe, and Ag. These major peaks confirm the incorporation of magnetite and silver nanoparticles within the activated carbon matrix. In addition, a homogenous dispersion of Fe and Ag can be seen on the surface of activated carbon for Mag@AC1-Ag and Mag@AC2-Ag samples (Fig. 3g, h).

Fourier transform infrared spectroscopy (FT-IR)

The FT-IR spectra of magnetite, Mag@AC1-Ag, and Mag@AC2-Ag samples are shown in Fig. 4. The wide peaks at around 3382, 3182, and 3212 cm^{-1} indicate the O–H stretching vibration mode of the hydroxyl groups. The peaks of O–H stretching vibrations are broader in the cases of Mag@AC1-Ag and Mag@AC2-Ag due to

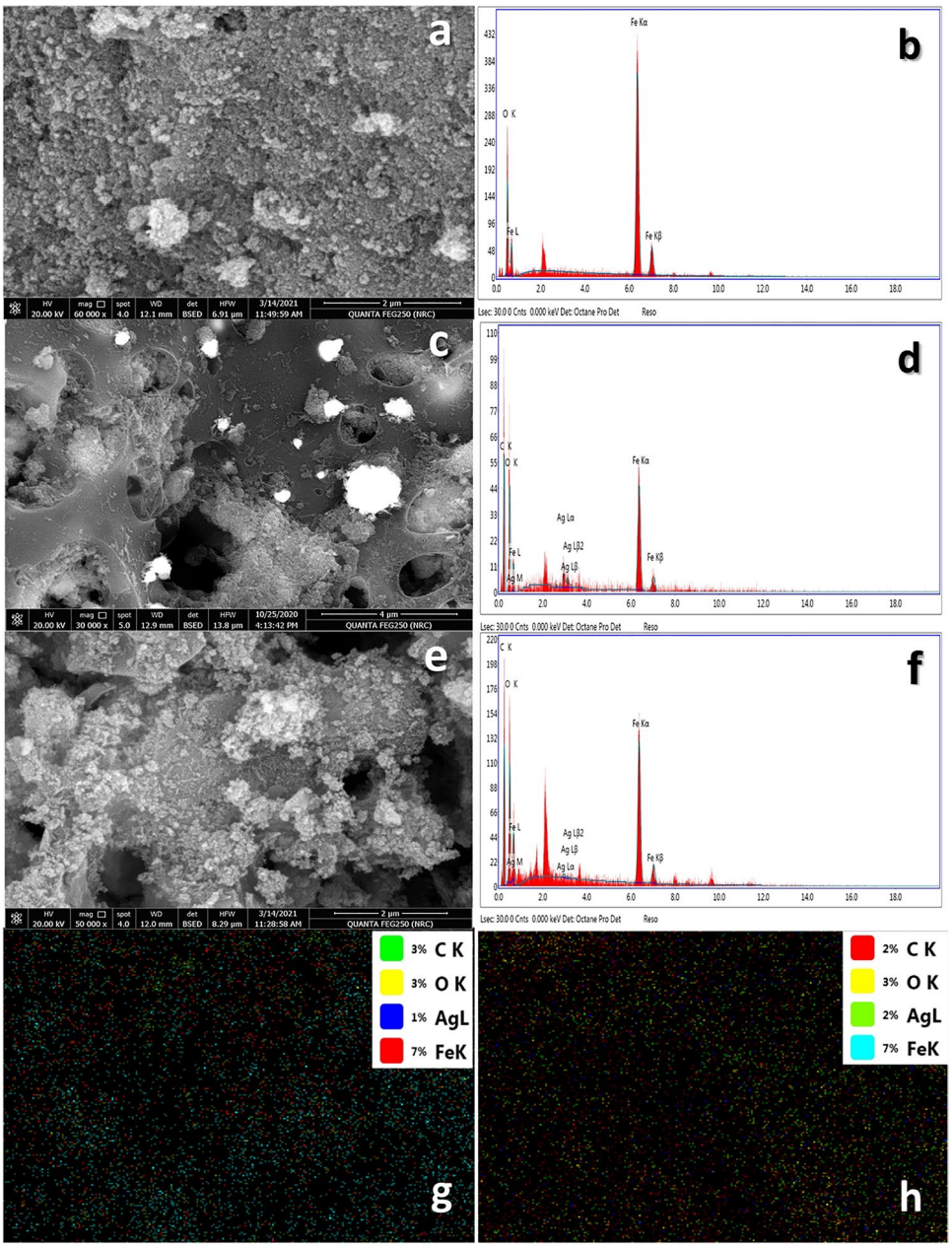

Fig. 3 SEM images and EDX survey for magnetite (**a**, **b**), Mag@AC1-Ag (**c**, **d**), and Mag@AC2-Ag (**e**, **f**), respectively, and elemental mapping for Mag@AC1-Ag (**g**) and Mag@AC2-Ag (**h**)

the carboxyl groups of activated carbon. As illustrated in the figure, the peaks at around 2927 and 2920 cm^{-1} are the C-H stretching vibration of the CH_3 groups in Mag@AC1-Ag and Mag@AC2-Ag, respectively, while the peaks at 1574 and 1568 cm^{-1} indicate the C = O stretching vibration of carboxyl/the aromatic ring C = C bond (Marzbani et al. 2016; Cai et al. 2021). In the IR spectra of Mag@AC1-Ag and Mag@AC2-Ag, the absorption peaks at 1381 and 1392 cm^{-1}, respectively, are assigned to symmetric stretching of -COO (Torab-Mostaedi et al. 2013; Li et al. 2017). Moreover, the presence of absorption peaks at about 544, 553, and 553 cm^{-1} in magnetite, Mag@AC1-Ag, and Mag@AC2-Ag, respectively, is assigned to the characteristic Fe–O stretching vibration, implying the existence of magnetite nanoparticles on the nanosorbents' surface (Jain et al. 2018).

Surface area and particle size analysis

The N_2 adsorption/desorption isotherms were determined for the prepared samples and are given in Figure S1 and Fig. 5. The samples of AC1 and AC2 exhibit type I isotherm (Figure S1), demonstrating that AC1 and AC2 have microporous structures (Li et al. 2014). On the other hand, magnetite, Mag@AC1-Ag,

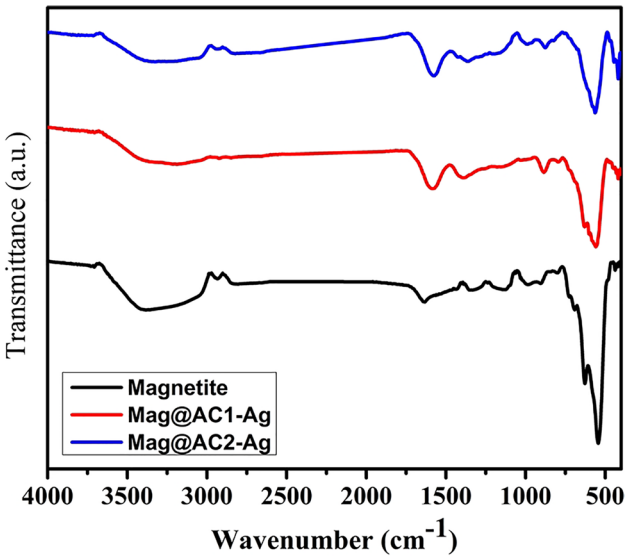

Fig. 4 FT-IR spectra of magnetite, Mag@AC1-Ag, and Mag@AC2-Ag

and Mag@AC2-Ag exhibit type IV isotherm, indicating the formation of mesoporous structures with a H1 hysteresis loop (Asghar et al. 2017). The hysteresis loop exists in the high relative region ($P/P_o > 0.6$) for magnetite and in $P/P_o > 0.50$ for Mag@AC1-Ag and Mag@AC2-Ag. At the lower pressure regions, the samples show the formation of a monolayer followed by the formation of multilayers. As shown in Fig. 5c, e, the amount of N_2 that has been adsorbed in the cases of Mag@AC1-Ag and Mag@AC2-Ag was low. It may be because magnetite and/or Ag nanoparticles covered the surface and filled the pores of the activated carbon. According to Fig. S1(b, d), AC1 and AC2 samples possessed internal pores that were predominantly micropores with a considerable amount of mesopores. Also, the results shown in Fig. 5b, d, and f indicated that magnetite, Mag@AC1-Ag, and Mag@AC2-Ag had pores inside, which were mainly mesopores. Therefore, the prepared nanosorbents may have excellent sorption performance.

The estimated BET surface areas, average pore diameters, and total pore volumes are listed in Table 1. As seen, the surface area of AC1 and AC2 decreased upon magnetite and

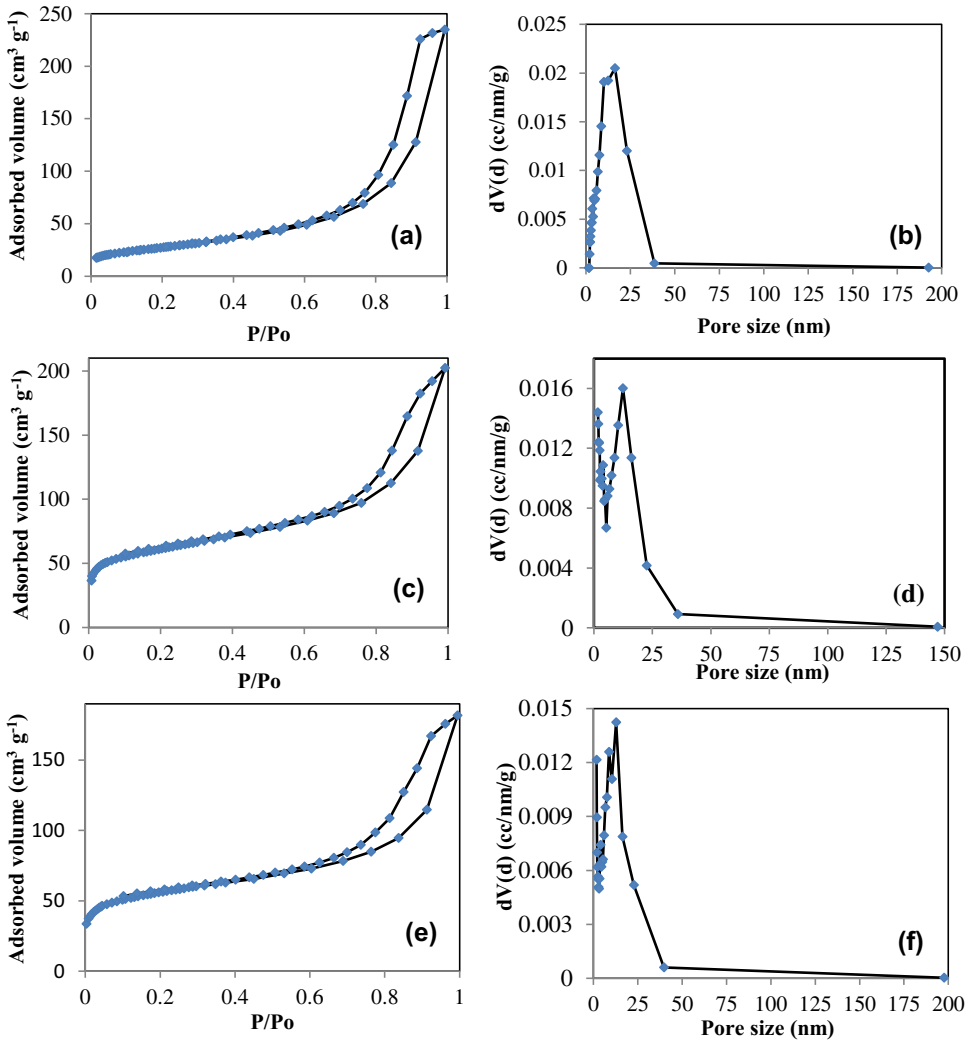

Fig. 5 N_2 adsorption–desorption isotherms and particle size distribution of magnetite (**a**, **b**), Mag@AC1-Ag (**c**, **d**), and Mag@AC2-Ag (**e**, **f**), respectively

Table 1 Calculated total specific surface area (S_{BET}), total pore volume (V_{tot}), and average pore diameter (D_p)

Sample	S_{BET} ($m^2\ g^{-1}$)	V_{tot} ($cm^3\ g^{-1}$)	D_P (nm)
AC1	426.95	0.21	1.96
AC2	364.39	0.19	2.04
Magnetite	97.53	0.36	14.91
Mag@AC1-Ag	220.9	0.31	5.67
Mag@AC2-Ag	203.6	0.28	5.52

silver nanoparticles incorporation in their structures. This may be due to some magnetite, or/and Ag nanoparticles have blocked the pores of activated carbon. Furthermore, it can be observed that Mag@AC1-Ag and Mag@AC2-Ag had high specific surface areas and rich pore structures, as revealed from SEM images as well. These findings suggest that Mag@AC1-Ag and Mag@AC2-Ag can be efficient sorbents for a variety of contaminants.

Batch sorption studies

Impact of initial pH

The impact of initial pH on the sorption of Pb^{2+} and Cd^{2+} ions by magnetite, Mag@AC1-Ag, and Mag@AC2-Ag was studied in the range of 2–7 to avoid Pb^{2+} and Cd^{2+} ion precipitation above pH > 7. The results are presented in Fig. 6a,

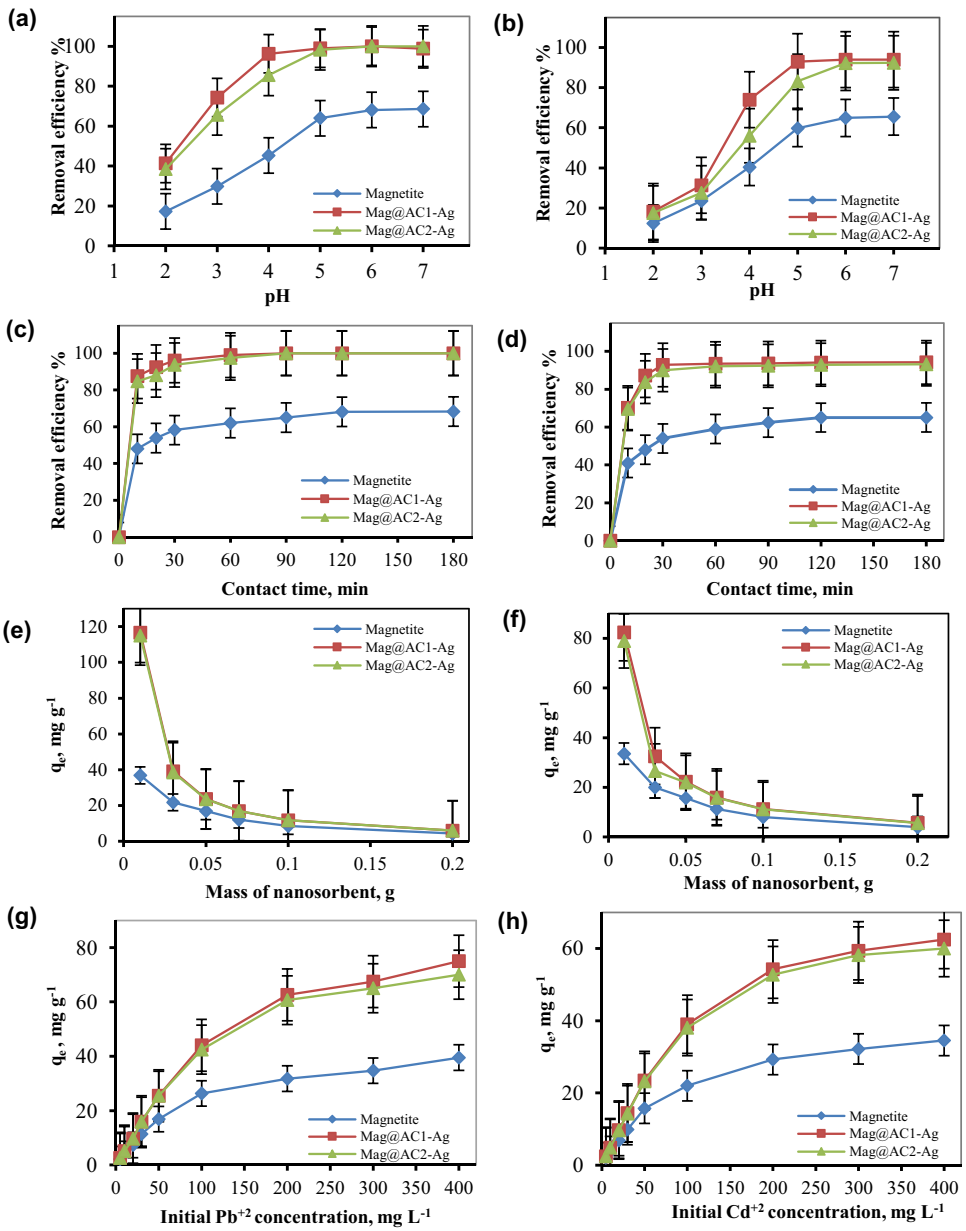

Fig. 6 Impact of initial pH, contact time, mass of nanosorbent, and initial metal concentration on the removal of Pb^{+2} (**a**, **c**, **e**, **g**) and Cd^{+2} (**b**, **d**, **f**, **h**) using magnetite, Mag@AC1-Ag, and Mag@AC2-Ag

b. As shown in the figure, the removal of Pb^{2+} and Cd^{2+} was improved by increasing the initial pH of the metal ion solution. At lower pH values, Pb^{2+} and Cd^{2+} ion removal decreased due to the increased H^+ ion competition for active sites. It would be suggested that at lower pH values, the nanosorbent surface is surrounded by H^+, and the surface becomes more positively charged, reducing the attraction between nanosorbents and metal ions. In contrast, when the pH increased, the functional groups on the surface of the nanosorbents, such as carboxylic acid groups, were deprotonated. Consequently, more negatively charged surfaces were created, leading to an electrostatic attraction between the positively charged metal ions and these negatively charged sorption sites; hence, their removal was increased. Based on these observations, in addition to the determined pHpzc values (section "Point of zero charge (pH_{pzc})"), it can be concluded that Pb^{2+} and Cd^{2+} removal might take place via several sorption processes (electrostatic attraction, surface complexation, ion-exchange, and coprecipitation). The same observation was also reported for the removal of Pb^{2+} and Cd^{2+} using mango seed biosorbent (Wang et al. 2022).

Impact of contact time

Pb^{2+} and Cd^{2+} ion removal was investigated at various time intervals of 10, 20, 30, 60, 90, 120, and 180 min. The other parameters, such as the initial Pb^{2+} or Cd^{2+} concentration (50 mg L^{-1}), nanosorbent mass (2 g L^{-1}), and temperature (25 °C) were kept constant. As revealed from Fig. 6c, d, the removal efficiency of Pb^{2+} and Cd^{2+} improved with increasing contact time until equilibrium was accomplished. The results demonstrated that the sorption process was very fast, where the prepared nanosorbents (Mag@AC1-Ag and Mag@AC2-Ag) showed rapid metal ion reduction in the first 10 min of contact time, followed by a progressive rise until equilibrium. The sorption onto Mag@AC1-Ag and Mag@AC2-Ag reached equilibrium in 60 min, after which no major change in the Pb^{2+} and Cd^{2+} removal percentage occurred. At the initial stages, the greater number of available sites on the nanosorbents' surfaces may have contributed to the higher sorption rates of Pb^{2+} and Cd^{2+}. The succeeding slower sorption was probably due to the contending among the Pb^{2+} or Cd^{2+} ions for the few available unsaturated sorption sites. As the nanosorbents' surfaces were saturated, the diffusion of Pb^{2+} or Cd^{2+} into the nanosorbents' bulk slowed down and the sorption rate diminished. To ensure complete sorption of Pb^{2+} and Cd^{2+} ions from the solution, the experiments were conducted for 120 min.

To check the stability of the prepared nanosorbents, the amounts of nanoparticles that might be released from the surface of activated carbon after equilibrium were measured. The results revealed that the amount of Ag ions released was between 0.32 and 0.35 mg L^{-1}) and that of Fe ions was between 0.095 and 0.92 mg L^{-1}), indicating the stability of the prepared nanosorbents.

Impact of nanosorbent mass

The effluence of nanosorbent mass on the Pb^{+2} and Cd^{+2} removal using magnetite, Mag@AC1-Ag, and Mag@AC2-Ag is shown in Fig. 6e, f. As observed, the sorption capacities diminished with an increase in the mass of nanosorbents. This may be due to particle interactions like aggregation driven on by the high nanosorbent mass, which result in a decrease in the nanosorbent's active surface area (Kakavandi et al. 2015).

Impact of Pb^{+2} or Cd^{+2} concentration

Figure 5g, h depict the impact of Pb^{+2} and Cd^{+2} concentrations on their removal by magnetite, Mag@AC1-0, and Mag@AC2-Ag at concentrations ranging from 5 to 400 mg L^{-1}, while all other process variables are held constant. The findings demonstrated that the sorption capacity increased along with the initial Pb^{+2} and Cd^{+2} concentrations. The sorption capacities raised from 2.13 to 39.51, 2.51 to 75, and 2.51 to 70 mg g^{-1} for Pb^{+2} by magnetite, Mag@AC1-Ag, and Mag@AC2-Ag, respectively. On the other hand, Cd^{+2} sorption capacities increased from 2.05 to 34.5, 2.46 to 62.5, and 2.45 to 60 mg g^{-1} for magnetite, Mag@AC1-Ag, and Mag@AC2-Ag, respectively. It can be noted that the Mag@AC1-Ag nanosorbent has a better sorption capacity towards Pb^{+2} and Cd^{+2} than the Mag@AC2-Ag sample. This can be attributed to its larger surface area, as revealed from BET analysis data. As the initial Pb^{+2} and Cd^{+2} concentrations rise, the mass transfer driving force overwhelms the barrier to Pb^{+2} and Cd^{+2} mass transfer from the solution to the nanosorbents. This causes greater contact between the nanosorbents' surface and Pb^{+2} and Cd^{+2}, hence increasing the sorption capacity. The preference of the nanosorbents for Pb^{+2} ions on the prepared nanosorbents is due to the fact that Pb has a smaller hydrated ionic radius than Cd (0.401 nm vs. 0.426 nm) (Yu et al. 2013).

Sorption kinetics

The sorption kinetics of Pb^{+2} and Cd^{+2} removal using magnetite, Mag@AC1-Ag, and Mag@AC2-Ag were elucidated using Lagergren pseudo-first-order, pseudo-second-order, and intra-particle diffusion models, and Table 2 lists the key parameters for each model.

Lagergren pseudo-first-order kinetics

As shown in Table 2, the estimated q_e values are not close to the experimental q_e values, revealing that the pseudo-first-order model (Figures S2 and S3) was not proper to

Table 2 Calculated parameters of the pseudo-first-order, pseudo-second-order, intra-particle diffusion, and Boyd models for Pb^{+2} and Cd^{+2} removal using magnetite, Mag@AC1-Ag, and Mag@AC2-Ag

Model	Metal ion	Parameters	Nanosorbent		
			Magnetite	Mag@AC1-Ag	Mag@AC2-Ag
Pseudo-first-order	Pb^{+2}	k_1	0.022	0.049	0.047
		$q_{e,\ calc.}$ (mg g^{-1})	5.65	4.98	5.80
		$q_{e,\ exp.}$ (mg g^{-1})	16.72	25.46	25.46
		R^2	0.9527	0.9937	0.9703
	Cd^{+2}	k_1	0.043	0.051	0.040
		$q_{e,\ calc.}$ (mg g^{-1})	11.36	4.43	3.94
		$q_{e,\ exp.}$ (mg g^{-1})	15.30	21.90	21.66
		R^2	0.8845	0.9239	0.9268
Pseudo-second-order	Pb^{+2}	k_2	0.009	0.027	0.016
		$q_{e,\ calc.}$ (mg g^{-1})	17.54	25.70	25.90
		$q_{e,\ exp.}$ (mg g^{-1})	16.72	25.46	25.46
		R^2	0.9994	1.0000	0.9999
	Cd^{+2}	k_2	0.008	0.024	0.019
		$q_{e,\ calc.}$ (mg g^{-1})	16.13	22.22	22.03
		$q_{e,\ exp.}$ (mg g^{-1})	15.30	21.90	21.66
		R^2	0.9996	0.9998	0.9999
Intra-particle diffusion	Pb^{+2}	k_d	1.083	0.938	0.942
		C	8.37	19.33	18.42
		R^2	0.9998	1	0.8841
	Cd^{+2}	k_d	1.317	2.304	2.079
		C	5.45	9.33	9.77
		R^2	0.9990	0.9583	0.9788
Boyd model	Pb^{+2}	R^2	0.9999	0.9933	0.8854
	Cd^{+2}	R^2	0.9965	0.9930	0.9976

explain the Pb^{+2} and Cd^{+2} sorption kinetics onto magnetite, Mag@AC1-Ag, and Mag@AC2-Ag nanosorbents.

Pseudo-second-order kinetics

The pseudo-second-order kinetics' results are shown in Figures S4 and S5, which illustrate the relationship between t/q_t and t for the Pb^{2+} and Cd^{+2} removal using magnetite, Mag@AC1-Ag, and Mag@AC2-Ag. It is evident that a straight line is used to depict the relationship. Table 2 also shows that the regression coefficient values are close to unity for Pb^{2+} and Cd^{2+} for all nanosorbents, and the estimated q_e values are very similar to those of the experimentally obtained q_e, revealing that the pseudo-second-order model is more appropriate to describe the kinetics of Pb^{2+} and Cd^{2+} sorption onto all nanosorbents.

Intra-particle diffusion model

The plots of the intra-particle diffusion model are shown in Fig. 7a, b. The plots are shown in Fig. 7a, b. The figure shows the presence of two stages during the Pb^{+2} and Cd^{+2}

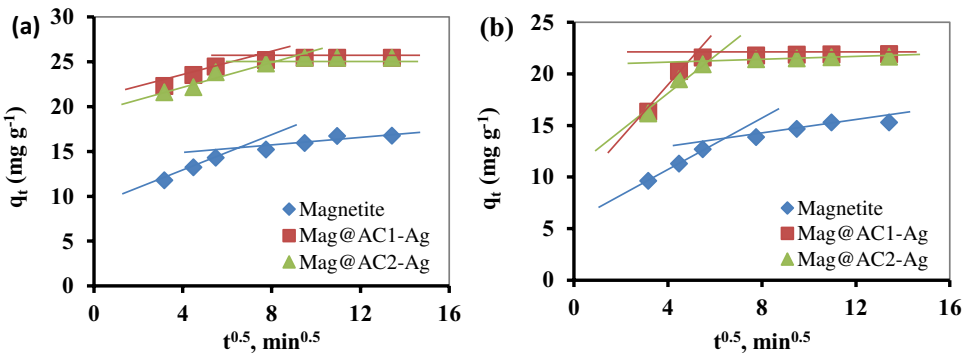

Fig. 7 Intra-particle diffusion plots for the removal of Pb^{+2} (**a**) and Cd^{+2} (**b**) using magnetite, Mag@AC1-Ag, and Mag@AC2-Ag

sorption onto magnetite, Mag@AC1-Ag, and Mag@AC2-Ag. The first stage represents the film diffusion ascribed to the external mass transport of Pb^{+2} and Cd^{+2} ions from the bulk solution to the nanosorbent surface. The second stage was related to the Pb^{+2} and Cd^{+2} ions' diffusion through the pores of nanosorbents, which became sluggish due to the decrease in the metal ions' concentration or the decrease of effective sorption sites on the nanosorbents (Jiang et al. 2018). If intra-particle diffusion is the only rate-limiting step, the graph of q_t vs. $t^{0.5}$ will be linear, and the line will intersect the origin. However, in the present case, the lines did not intersect at the origin, which indicated that the rate-limiting step of the sorption of Pb^{+2} and Cd^{+2} was simultaneously controlled by film and intra-particle diffusion (Hu et al. 2020).

Boyd model

It is clear from the intra-particle diffusion investigation that the process of Pb^{+2} and Cd^{+2} removal using magnetite, Mag@AC1-Ag, and Mag@AC2-Ag was a multi-step process. However, there is still a consideration regarding the step that governs the overall rate of sorption. For that reason, the mathematical expression of the Boyd model was applied to the sorption data in order to define the actual rate-limiting step. The characteristics of Boyd plots provided essential data about whether film or intra-particle diffusion identified the rate-limiting step. When the obtained plot is linear and traverses the origin, intra-particle diffusion is thought to be the rate-limiting mechanism. Nevertheless, if the plot does not traverse the origin, external mass transfer (film diffusion) limits the overall rate of the Pb^{+2} and Cd^{+2} removal process. As shown in Figures S6 and S7, the plots were linear at the initial stage of sorption (R^2 is illustrated in Table 2). The obtained plots for the Boyd model did not traverse the origin, revealing that the Pb^{+2} and Cd^{+2} sorption onto the prepared nanosorbents at the beginning of the sorption process was regulated by film diffusion (Ofomaja 2010).

Sorption isotherms

Different isotherms were used to express the relationship between Pb^{+2} and Cd^{+2} ions' equilibrium concentrations in the solid and liquid phases, including the Langmuir, Freundlich, D-R, and Temkin isotherms.

Langmuir isotherm

The Langmuir isotherm presumes that a sorbent contains a limited number of binding sites of identical energy. One molecule is sorbed by each site, resulting in a single monolayer. Figures S8 and S9 show the plots of C_e/q_e vs. C_e, whereas the values of q_{max}, k_L, and R^2 are listed in Table 3. As observed, the q_{max} values were 41.67, 72.99, and 68.97 mg g^{-1} for Pb^{+2} and 37.04, 62.50, and 60.61 mg g^{-1} for Cd^{+2} using magnetite, Mag@AC1-Ag, and Mag@AC2-Ag, respectively. The sorption capacities of the prepared nanosorbents followed the order: Mag@AC1-Ag > Mag@AC2-Ag > magnetite.

To assess the feasibility and favorability of the Pb^{+2} and Cd^{+2} sorption, the separation factor (R_L) was estimated as follows:

$$R_L = \frac{1}{1 + K_L C_i} \tag{18}$$

R_L value specifies whether the isotherm is unfavorable ($R_L > 1$), favorable ($0 < R_L < 1$), linear ($R_L = 1$), or irreversible ($R_L = 0$). As displayed in Table 3, the R_L values were between 0 and 1, indicating a favorable Pb^{+2} and Cd^{+2} sorption process onto magnetite, Mag@AC1-Ag, and Mag@AC2-Ag.

Freundlich isotherm

According to the Freundlich isotherm, sorbents have heterogeneous surfaces with various sorption potential locations. Additionally, it presumes that stronger binding sites are firstly occupied and that binding strength diminishes as occupancy increases. The plots of log q_e vs. log C_e are displayed in Figures S10 and S11, whereas n and K_F values are listed in Table 3. In the case of Mag@AC1-Ag, the higher values of K_F than those of magnetite and Mag@AC2-Ag indicated the high sorption efficacy of Mag@AC1-Ag. The value of 1/n quantifies how heterogeneous a surface is, where the closer the value of 1/n is to zero, the more heterogeneous the surface. According to the table, 1/n values vary from 0 to 1, which reflects the magnetite, Mag@AC1-Ag, and Mag@AC2-Ag surfaces' heterogeneity.

As can be noticed from the table, the values of (R^2) for the Langmuir model were higher than those for the Freundlich model, thus implying that the Langmuir model better suited the experimental sorption data, thereby indicating monolayer sorption. This also suggests that the surfaces of the prepared nanosorbents are homogeneous in nature.

Dubinin–Radushkevich isotherm (D-R)

The D-R model discriminates between chemical and physical sorption processes. The obtained plots of ln q_e vs. ε^2 are displayed in Figures S12 and S13. The value of E (Table 3) reveals the sorption mechanism, which is either physisorption if E is less than 8 kJ mol^{-1} or chemisorption if E is between 8 and 16 kJ mol^{-1}. The values of E in this study were less than 8 kJ mol^{-1}, indicating that the sorption process of Pb^{+2} and Cd^{+2} onto magnetite, Mag@AC1-Ag, and Mag@AC2-Ag may have been dominated by physisorption.

Table 3 Parameters of the Langmuir, Freundlich, Dubinin-Radushkevich (D–R), and Temkin isotherm models for the sorption of Pb^{+2} and Cd^{+2} onto magnetite, Mag@AC1-Ag, and Mag@AC2-Ag

Isotherm model	Metal ion	Parameters	Nanosorbent		
			Magnetite	Mag@AC1-Ag	Mag@AC2-Ag
Langmuir	Pb^{+2}	K_L (L mg^{-1})	0.044	0.320	0.340
		q_{max} (mg g^{-1})	41.67	72.99	68.97
		R^2	0.9925	0.9946	0.9964
		R_L	0.3160	0.0076	0.0073
	Cd^{+2}	K_L (L mg^{-1})	0.041	0.150	0.165
		q_{max} (mg g^{-1})	37.04	62.50	60.61
		R^2	0.9964	0.9974	0.9979
		R_L	0.336	0.110	0.118
Freundlich	Pb^{+2}	K_F	12.03	28.11	26.10
		1/n	0.201	0.177	0.181
		R^2	0.9658	0.9856	0.9732
	Cd^{+2}	K_F	2.85	10.05	9.33
		1/n	0.475	0.374	0.381
		R^2	0.9542	0.9371	0.9364
Dubinin-Radushkevich (D–R)	Pb^{+2}	K_{D-R}	35.94	68.70	65.74
		$\beta*10^{-3}$	0.114	0.014	0.021
		E (kJ mol^{-1})	2.09	5.94	4.87
		R^2	0.7845	0.9113	0.9465
	Cd^{+2}	K_{D-R}	33.11	59.44	57.77
		$\beta*10^{-3}$	0.195	0.038	0.044
		E (kJ mol^{-1})	1.60	3.63	3.37
		R^2	0.9483	0.9485	0.9567
Temkin	Pb^{+2}	b_T (kJ mol^{-1})	0.387	0.244	0.252
		A_T	1.19	5.82	4.84
		R^2	0.9386	0.9867	0.9854
	Cd^{+2}	b_T (kJ mol^{-1})	0.412	0.312	0.314
		A_T	0.85	8.13	6.68
		R^2	0.9775	0.9826	0.9842

Temkin isotherm

According to the Temkin isotherm, interactions between the sorbent and the sorbate cause the sorption energy to decrease linearly with surface coverage. The values of A_T and b_T can be estimated from the q_e vs. ln C_e plot (Figures S14 and S15). As given in Table 3, the values of b_T ranged from 0.189 to 0.387 kJ mol^{-1}. Weak electrostatic interactions can be distinguished by b_T values that are less than 20 kJ mol^{-1}. Therefore, these results further emphasized that the sorption of Pb^{+2} and Cd^{+2} onto magnetite, Mag@AC1-Ag, and Mag@AC2-Ag showed good compatibility with the physisorption process (Mohammadnezhad et al. 2017).

Thermodynamics studies

The temperature impact on the Pb^{2+} and Cd^{2+} sorption onto the prepared nanosorbents was evaluated. With rising temperature, it was observed that the percentage of metal ions removed increased. This revealed that the Pb^{2+} and Cd^{2+}sorption process onto magnetite, Mag@AC1-Ag, and Mag@AC2-Ag was endothermic in nature. The plots of ln K_d vs. 1/T are displayed in Figures S16 and S17. The values of the thermodynamic parameters are tabulated in Table 4. The negative ΔG values for the sorption onto Mag@AC1-Ag and Mag@AC2-Ag reflected the spontaneous nature of the sorption process. However, in the case of magnetite, ΔG is positive, demonstrating that the Pb^{+2} and Cd^{+2} sorption is unfavorable. As noticed, the absolute values of ΔG raised as the temperature rose, implying that the high temperatures were preferred for the sorption of Pb^{+2} and Cd^{+2} onto Mag@AC1-Ag and Mag@AC2-Ag. The positive values of ΔH revealed the endothermic character of the sorption process. As noticed in Table 4, the ΔH values were between 38.99 and 65.71 kJ mol^{-1} for Mag@AC1-Ag and Mag@AC2-Ag, demonstrating a physico-chemical sorption process of the studied metals onto these nanosorbents (Liu and Liu 2008). On the other hand, the ΔH values for magnetite were less

Table 4 Thermodynamic parameters for sorption of Pb^{+2} and Cd^{+2} onto magnetite, Mag@AC1-Ag, and Mag@AC2-Ag

Metal ion	Nanosorbent	ΔH (kJ mol^{-1})	ΔS (J mol^{-1} K^{-1})	ΔG (kJ mol^{-1})				R^2
				298 K	308 K	318 K	328 K	
Pb^{+2}	Magnetite	7.35	20.22	1.325	1.123	0.921	0.718	0.9258
	Mag@AC1-Ag	65.71	228.84	−2.483	−4.771	−7.060	−9.348	0.9200
	Mag@AC2-Ag	58.39	202.46	−1.945	−3.970	−5.994	−8.019	0.9542
Cd^{+2}	Magnetite	6.01	19.67	0.152	−0.045	−0.241	−0.439	0.9939
	Mag@AC1-Ag	45.31	169.33	−5.152	−6.846	−8.539	−10.232	0.9833
	Mag@AC2-Ag	38.99	146.86	−4.774	−6.243	−7.711	−9.180	0.9783

than 20 kJ mol^{-1}, denoting a physisorption process (Liu and Liu 2008). Furthermore, the positive ΔS values suggested that the randomness raised at the solid/liquid interface during the Pb^{+2} and Cd^{+2} sorption onto magnetite, Mag@AC1-Ag, and Mag@AC2-Ag.

Desorption and reusability studies

The potential for sorbents' regeneration has gained economic significance due to the high cost of wastewater treatment systems. For desorption process, 10 mL of 0.1 mol L^{-1} HCl was mixed with 0.05 g Pb- or Cd-loaded nanosorbent for 1 h at 25 °C. HCl is universally employed for desorbing many metal ions from the sorbents since it is frequently used in industry, metal ions are soluble in it, and it is relatively inexpensive (Jain et al. 2018). The desorbed Pb^{+2} and Cd^{+2} ions were evaluated, and the desorption efficiencies for Pb^{+2} using HCl were 93.33, 97.2, and 96.6%, while for Cd^{+2}, they were 92.56, 95.7, and 94.4% for magnetite, Mag@AC1-Ag, and Mag@AC2-Ag, respectively. The sorption–desorption for Pb^{+2} and Cd^{+2} was performed repetitively, up to five cycles. As illustrated in Fig. 8, after each cycle, the sorption capacity was slightly reduced, indicating that the nanosorbents had good regeneration capability. For example, in the case of Mag@AC1-Ag, the sorption capacities of the first, second, and 3rd cycles for Pb^{+2} were 25.45, 24.20, and 22.80 mg g^{-1}, respectively, and for Cd^{+2}, they were 23.23, 22.00, and 20.65 mg g^{-1}, respectively.

Comparison with other sorbents

The characteristics of some adsorbents and their sorption capacities towards Pb^{+2} and Cd^{+2} are recorded in Table S1. The difference in the sorption capacities was a consequence of the distinctive characteristics of each adsorbent concerning the main functional groups, surface area, pore volume, etc. As could be seen, Mag@AC1-Ag and Mag@AC2-Ag exhibited good sorption capacities when compared to other sorbents.

Antimicrobial activity of nanosorbents

The antibacterial activity of magnetite, Mag@AC1-Ag, Mag@AC2-Ag and $AgNO_3$ was examined by the zone of inhibition method against both fecal coliform (gram-negative) and *Bacillus subtilis* (gram-positive). Figure 9 and Table 5 display the results. As seen, magnetite had a little antibacterial activity against both strains. On the other hand, Mag@AC1-Ag, Mag@AC2-Ag, and $AgNO_3$ exhibited high antimicrobial activity against both fecal coliform and *Bacillus subtilis*; however, they were more active against gram-negative than positive one. This could be as a result of the two strains' cell walls having different compositions (Jemal et al. 2017). In contrast to gram-negative bacteria, which have cell walls made up of a thin peptidoglycan layer and a lipopolysaccharide layer, gram-positive bacteria have thick peptidoglycan layers made of

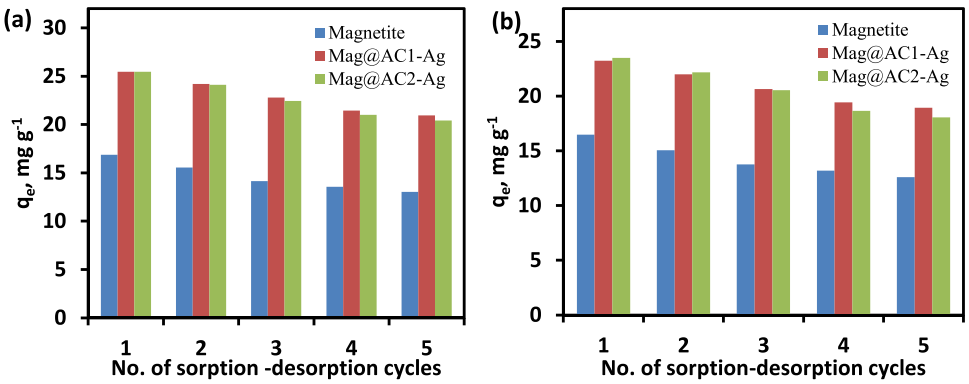

Fig. 8 Reusability of magnetite, Mag@AC1-Ag, and Mag@AC2-Ag for the removal of Pb^{+2} (**a**) and Cd^{+2} (**b**)

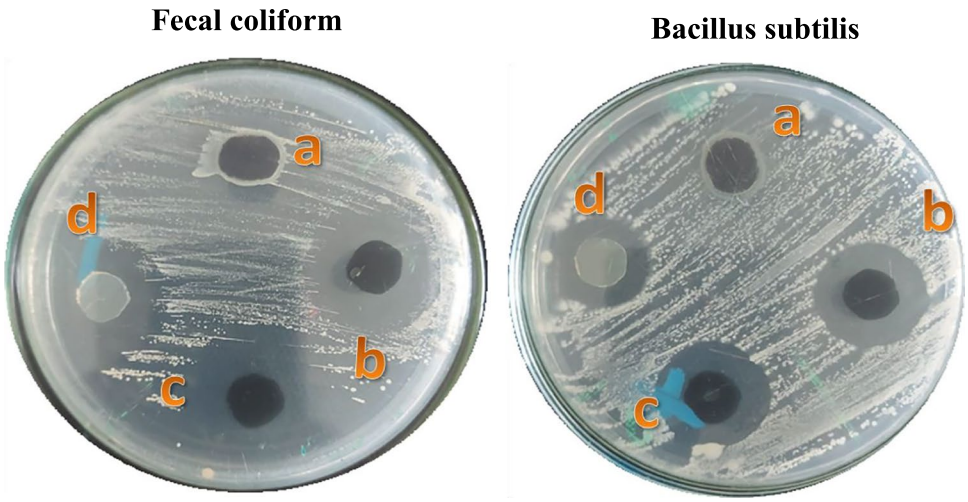

Fig. 9 The inhibition zones of (a) magnetite, (b) Mag@AC2-Ag, (c) Mag@AC1-Ag, and (d) $AgNO_3$ against fecal coliform and *Bacillus subtilis*

linear polysaccharide chains cross-linked via short peptides, creating a three-dimensional rigid structure that makes nanosorbent penetration difficult. The lipopolysaccharides are comprised of negatively charged polysaccharides and covalently linked lipids, providing a poor permeability barrier to the positively charged nanosorbents due to the presence of AgNPs. Silver nanocomposites demonstrated significantly higher effluent disinfection efficiency and antibacterial activity against a wide range of microorganisms (Najafpoor et al. 2020). Upon contact with microbes, the silver nanocomposites are believed to be oxidized into Ag^+ ions that destabilize the penetrability and respiration cellular functions and enter the microorganisms (Furlan et al. 2017), affecting intracellular processes such as DNA, RNA, and protein synthesis. This leads to cell death or cellular inactivation (Franci et al. 2015; Notriawan et al. 2013). Furthermore, other pathways have been identified, such as the interaction of silver nanocomposite with bacterial cell surface structures and the interaction of liberated Ag ions with sulfur and phosphorous in cell macromolecules (Ghaseminezhad et al. 2018). AgNPs can demonstrate their antibacterial action via the creation of reactive oxygen species, which can break down DNA and proteins in bacterial cells (Azócar et al. 2019).

Table 5 also displays the antibacterial activities of some other reported studies. It can be remarked that the values of the inhibition zones of Mag@AC1-Ag and Mag@AC2-Ag were smaller than those obtained by Truong et al. (2022) and Altintig et al. (2022) for gram-positive bacteria but higher for gram-negative bacteria. On the other hand, they were

Table 5 Inhibition zone diameters of Mag@AC1-Ag, Mag@AC2-Ag, and different materials against different bacterial strains

Material	Bacterial strains		Inhibition zone (mm)	Reference
	Gram negative	Gram positive		
$Co_{0.7}Zn_{0.3}Fe_2O_4$/PET/Ag	*Escherichia coli*	-	12.50	Jalali et al. (2017)
	-	*Staphylococcus aureus*	11.50	
AgNP-AC	*Escherichia coli*	-	18.00	Karthik and Radha (2016)
	-	*Bacillus subtilis*	17.00	
AgAC	*Escherichia coli*	-	10.60	Karadirek and Okkay (2019)
	-	*Staphylococcus aureus*	13.38	
GO–Ag NPs	*Escherichia coli*	-	20.00	Truong et al. (2022)
	-	*Staphylococcus aureus*	31.00	
AgNPAC	*Escherichia coli*	-	24.10	Altintig et al. (2022)
	-	*Staphylococcus aureus*	34.10	
AgNPs	*Pseudomonas aeruginosa*	-	24.40	Gopinathan and Balasubramanian (2022)
	-	*Bacillus cereus*	18.90	
Mag@AC1-Ag	Fecal coliform	-	28.00	This study
	-	*Bacillus subtilis*	25.00	
Mag@AC2-Ag	Fecal coliform	-	26.00	This study
	-	*Bacillus subtilis*	22.00	

Table 6 Removal of Pb^{+2} and Cd^{+2} from different water samples using magnetite, Mag@AC1-Ag, and Mag@AC2-Ag ($n=3$)

Sample	Nanosorbent	Pb^{+2} (mg L^{-1})		R%	RSD%	Cd^{+2} (mg L^{-1})		R%	RSD%
		Before treatment	After treatment			Before treatment	After treatment		
Tap water	Magnetite	50.90	16.79	67.01	1.77	49.00	17.75	63.78	2.29
	Mag@AC1-Ag	50.90	0.29	99.44	3.22	49.00	3.13	93.61	2.84
	Mag@AC2-Ag	50.90	0.39	99.23	2.03	49.00	3.700	92.45	3.38
Nile water	Magnetite	50.90	17.23	66.15	1.60	49.00	18.55	62.14	1.35
	Mag@AC1-Ag	50.90	0.76	98.50	2.66	49.00	3.79	92.27	4.12
	Mag@AC2-Ag	50.90	0.91	98.20	2.47	49.00	4.37	91.08	1.67
Groundwater	Magnetite	50.90	17.61	65.40	1.65	49.00	19.13	60.96	1.88
	Mag@AC1-Ag	50.90	0.97	98.10	1.19	49.00	4.31	91.20	3.51
	Mag@AC2-Ag	50.90	1.19	97.67	0.84	49.00	4.90	90.00	1.67

higher than the other materials for both strains, demonstrating the effectiveness of Mag@AC1-Ag and Mag@AC2-Ag as antibacterial materials.

Application of real samples

To assess the analytical applicability of the produced nanosorbents for water remediation, magnetite, Mag@AC1-Ag, and Mag@AC2-Ag nanosorbents were applied to remove Pb^{+2} and Cd^{+2} ions from spiked water samples, including tap water, Nile water, and groundwater. The samples were spiked with Pb^{+2} and Cd^{+2} metal ions at a concentration of ≈ 50 mg L^{-1}. The values of removal percentages (R%) and RSD% are given in Table 6. As shown, the higher values of the removal percentages of Pb^{+2} and Cd^{+2} from the tap, Nile, and groundwater samples indicated the applicability of the Mag@AC1-Ag and Mag@AC2-Ag nanosorbents as effective and eco-friendly sorbents to remove Pb^{+2} and Cd^{+2} ions from real samples. Tap water, as the clean matrix, resulted in the highest removal percentage compared to river water and groundwater, whose matrices were more complex than tap water (Nodeh et al. 2019).

Conclusions

Using commonly available materials and equipment, eco-friendly mesoporous nanosorbents were produced via the incorporation of magnetite and antimicrobial silver nanoparticles into activated carbon-based palm shell. The obtained isotherms of the prepared samples, including magnetite, Mag@AC1-Ag, and Mag@AC2-Ag, proved the formation of mesoporous structures. Also, they have a pseudo-spherical shape with particle sizes in the range of 6–10, 4–10, and 8–14 nm for magnetite, Mag@AC1-Ag, and Mag@AC2-Ag, respectively. The prepared nanosorbents were characterized and employed for the Pb^{+2} and Cd^{+2} removal from water and wastewater. The sorption capacity of Pb^{2+} was greater than that of Cd^{2+} because Pb has a smaller hydrated ionic radius. The experimental data for Pb^{+2} and Cd^{+2} removal fitted well with the Langmuir isotherm. According to the kinetic studies, the pseudo-second-order model provided a superior fit to the obtained data. In addition, the thermodynamic parameters revealed that Pb^{+2} and Cd^{+2} removal using the nanosorbents was endothermic and spontaneous. The results further demonstrated the acceptable stability and significant recyclability of the nanosorbents. They exhibited higher efficiency for wastewater disinfection, where they showed strong antibacterial activity against fecal coliform and *Bacillus subtilis*. Furthermore, the prepared nanosorbents can be considered potential eco-friendly sorbents since they exhibited efficient elimination of toxic Pb^{+2} and Cd^{+2} ions from real samples, such as tap water, Nile water, and groundwater. In summary, the findings demonstrated that these eco-friendly nanosorbents would make better candidates for wastewater treatment.

Supplementary Information The online version contains supplementary material available at https://doi.org/10.1007/s11356-023-26000-w.

Acknowledgements The authors are grateful to Soil, Water and Environment Research Institute, Agriculture Research Centre for using the resources in this study and to the National Research Centre, Giza, for the equipment facilities.

Author contribution The study's conception and design were contributed to by all authors. Data collection and sample analysis: Eman R. Zaki. Manuscript preparation and data analysis: Omnia I. Ali and Eman R. Zaki. The final manuscript was read and approved by all authors.

Funding Open access funding provided by The Science, Technology & Innovation Funding Authority (STDF) in cooperation with The Egyptian Knowledge Bank (EKB).

Data availability Raw data are available upon request.

Declarations

Ethics approval This work does not contain any investigations with human participants or animals performed by any of the authors.

Consent to participate Not applicable.

Consent to publish Not applicable.

Competing interests The authors declare no competing interests.

References

Abatal M, Olguin MT, Anastopoulos I, et al (2021) Comparison of heavy metals removal from aqueous solution by Moringa oleifera leaves and seeds. Coatings 11. https://doi.org/10.3390/coatings11050508

Adinata D, Daud WMA, Aroua MK (2007) Preparation and characterization of activated carbon from palm shell by chemical activation with K_2CO_3. Bioresour Technol 98:145–149

Akperov EO, Akperov OH (2019) The wastage of the cotton stalks (Gossypium hirsutum L.) as low-cost adsorbent for removal of the Basic Green 5 dye from aqueous solutions. Appl Water Sci 9:1–9

Altintig E, Sarıcı B, Karataş S (2022) Prepared activated carbon from hazelnut shell where coated nanocomposite with Ag^+ used for antibacterial and adsorption properties. Environ Sci Pollut Res Int 30(5):13671–13687. https://doi.org/10.1007/s11356-022-23004-w

Asghar K, Qasim M, Dharmapuri G, Das D (2017) Investigation on a smart nanocarrier with a mesoporous magnetic core and thermo-responsive shell for co-delivery of doxorubicin and curcumin: a new approach towards combination therapy of cancer. RSC Adv 7:28802–28818. https://doi.org/10.1039/c7ra03735j

Asuquo E, Martin A, Nzerem P et al (2017) Adsorption of Cd (II) and Pb (II) ions from aqueous solutions using mesoporous activated carbon adsorbent: equilibrium, kinetics and characterisation studies. J Environ Chem Eng 5:679–698

Azócar MI, Alarcón R, Castillo A et al (2019) Capping of silver nanoparticles by anti-inflammatory ligands: antibacterial activity and superoxide anion generation. J Photochem Photobiol B Biol 193:100–108

Baby R, Saifullah B, Hussein MZ (2019) Palm Kernel Shell as an effective adsorbent for the treatment of heavy metal contaminated water. Sci Rep 9:1–11

Bahadır Z, Bulut VN, Ozdes D et al (2014) Separation and preconcentration of lead, chromium and copper by using with the combination coprecipitation-flame atomic absorption spectrometric determination. J Ind Eng Chem 20:1030–1034

Bastami TR, Entezari MH (2012) Activated carbon from carrot dross combined with magnetite nanoparticles for the efficient removal of p-nitrophenol from aqueous solution. Chem Eng J 210:510–519

Blachnio M, Derylo-Marczewska A, Charmas B et al (2020) Activated carbon from agricultural wastes for adsorption of organic pollutants. Molecules 25:1–35. https://doi.org/10.3390/molecules25215105

Cai T, Du H, Liu X et al (2021) Insights into the removal of Cd and Pb from aqueous solutions by NaOH–EtOH-modified biochar. Environ Technol Innov 24:102031

Chandana L, Krushnamurty K, Suryakala D, Subrahmanyam C (2020) Low-cost adsorbent derived from the coconut shell for the removal of hexavalent chromium from aqueous medium. Mater Today Proc 26:44–51

Cullity BD (1956) Elements of X-ray diffraction. Addison-Wesely Publishing Company Inc, Massachusetts

Dave PN, Chopda LV (2014) Application of iron oxide nanomaterials for the removal of heavy metals. J Nanotechnol 2014. https://doi.org/10.1155/2014/398569

El Zayat M, Smith E (2013) Modeling of heavy metals removal from aqueous solution using activated carbon produced from cotton stalk. Water Sci Technol 67:1612–1619

Fatimah I, Fadillah G, Yudha SP (2021) Synthesis of iron-based magnetic nanocomposites: a review. Arab J Chem 14:103301. https://doi.org/10.1016/j.arabjc.2021.103301

Franci G, Falanga A, Galdiero S et al (2015) Silver nanoparticles as potential antibacterial agents. Molecules 20:8856–8874

Furlan PY, Fisher AJ, Furlan AY, et al (2017) Magnetically recoverable and reusable antimicrobial nanocomposite based on activated carbon, magnetite nanoparticles, and silver nanoparticles for water disinfection. Inventions 2. https://doi.org/10.3390/inventions2020010

Furlan PY, Melcer ME (2014) Removal of aromatic pollutant surrogate from water by recyclable magnetite-activated carbon nanocomposite: an experiment for general chemistry. J Chem Educ 91:1966–1970

Geneti ST, Mekonnen GA, Murthy HC, et al (2022) Biogenic synthesis of magnetite nanoparticles using leaf extract of Thymus schimperi and their application for monocomponent removal of chromium and mercury ions from aqueous solution. J Nanomater 2022. https://doi.org/10.1155/2022/5798824

Ghaseminezhad SM, Shojaosadati SA, Meyer RL (2018) Ag/Fe_3O_4 nanocomposites penetrate and eradicate S. aureus biofilm in an in vitro chronic wound model. Colloids Surf B Biointerfaces 163:192–200

Gopinathan M, Balasubramanian M (2022) Green synthesis and characterization of silver nanoparticles using Heliotropium indicum L. leaves extract and antimicrobial activity. J Adv Sci Res 13:365–373

Hu B, Li Y, Jiang L et al (2020) Influence of microplastics occurrence on the adsorption of 17β-estradiol in soil. J Hazard Mater 400:123325. https://doi.org/10.1016/j.jhazmat.2020.123325

Issabayeva G, Aroua MK, Sulaiman NMN (2006) Removal of lead from aqueous solutions on palm shell activated carbon. Bioresour Technol 97:2350–2355

Jain M, Yadav M, Kohout T et al (2018) Development of iron oxide/activated carbon nanoparticle composite for the removal of Cr(VI), Cu(II) and Cd(II) ions from aqueous solution. Water Resour Ind 20:54–74. https://doi.org/10.1016/j.wri.2018.10.001

Jalali SAH, Allafchian A, Bahramian H, Amiri R (2017) An antibacterial study of a new magnetite silver nanocomposite. J Environ Chem Eng 5:5786–5792

Jemal K, Sandeep B V, Pola S (2017) Synthesis, characterization, and evaluation of the antibacterial activity of Allophylus serratus leaf and leaf derived callus extracts mediated silver nanoparticles. J Nanomater 2017. https://doi.org/10.1155/2017/4213275

Jiang L, Liu Y, Zeng G et al (2018) Adsorption of 17B-estradiol by graphene oxide: effect of heteroaggregation with inorganic nanoparticles. Chem Eng J 343:371–378. https://doi.org/10.1016/j.cej.2018.03.026

Kakavandi B, Kalantary RR, Jafari AJ et al (2015) Pb(II) adsorption onto a magnetic composite of activated carbon and superparamagnetic Fe_3O_4 nanoparticles: experimental and modeling study. Clean – Soil Air Water 43:1157–1166. https://doi.org/10.1002/clen.201400568

Karadirek Ş, Okkay H (2019) Ultrasound assisted green synthesis of silver nanoparticle attached activated carbon for levofloxacin adsorption. J Taiwan Inst Chem Eng 105:39–49

Karthik C, Radha KV (2016) Silver nanoparticle loaded activated carbon: an escalated nanocomposite with antimicrobial property. Orient J Chem 32:735–741

Khajeh M (2011) Response surface modelling of lead pre-concentration from food samples by miniaturised homogenous liquid–liquid solvent extraction: Box-Behnken design. Food Chem 129:1832–1838

Kyi PP, Quansah JO, Lee C, Moon J (2020) The removal of crystal violet from textile wastewater using palm kernel shell-derived biochar. Appl Sci 10. https://doi.org/10.3390/app10072251

Lee PC, Meisel D (1982) Adsorption and surface-enhanced Raman of dyes on silver and gold sols - The Journal of Physical Chemistry (ACS Publications). J Phys Chem 60439:3391–3395

Li J, Ren Z, Ren Y et al (2014) Activated carbon with micrometer-scale channels prepared from luffa sponge fibers and their application for supercapacitors. RSC Adv 4:35789–35796. https://doi.org/10.1039/c4ra04073b

Li B, Yang L, Wang C et al (2017) Adsorption of Cd(II) from aqueous solutions by rape straw biochar derived from different modification processes. Chemosphere 175:332–340

Li C, Zhou K, Qin W et al (2019) A review on heavy metals contamination in soil: effects, sources, and remediation techniques. Soil Sediment Contam an Int J 28:380–394

Liu Y, Liu YJ (2008) Biosorption isotherms, kinetics and thermodynamics. Sep Purif Technol 61:229–242. https://doi.org/10.1016/j.seppur.2007.10.002

Marzbani P, Resalati H, Ghasemian A, Shakeri A (2016) Surface modification of talc particles with phthalimide: study of composite structure and consequences on physical, mechanical, and optical properties of deinked pulp. BioResources 11:8720–8738. https://doi.org/10.15376/biores.11.4.8720-8738

Mezgebe B, Sahle-Demessie E, Sorial GA (2020) Disinfection byproducts in drinking water: formation, characterization, control technologies. In: Ahuja S, Loganathan BG (eds) Contaminants in Our Water: Identification and Remediation Methods. ACS Publications, Washington, DC, pp 119–142

Mia S, Dijkstra FA, Singh B (2017) Aging induced changes in biochar's functionality and adsorption behavior for phosphate and ammonium. Environ Sci Technol 51:8359–8367

Mohamed EF, El-Hashemy MA, Abdel-Latif NM, Shetaya WH (2015) Production of sugarcane bagasse-based activated carbon for formaldehyde gas removal from potted plants exposure chamber. J Air Waste Manag Assoc 65:1413–1420. https://doi.org/10.1080/10962247.2015.1100141

Mohammadnezhad G, Soltani R, Abad S, Dinari M (2017) A novel porous nanocomposite of aminated silica MCM-41 and nylon-6: isotherm, kinetic, and thermodynamic studies on adsorption of Cu(II) and Cd(II). Appl Polym 45383:1–12. https://doi.org/10.1002/app.45383

Najafpoor A, Norouzian-Ostad R, Alidadi H et al (2020) Effect of magnetic nanoparticles and silver-loaded magnetic nanoparticles on advanced wastewater treatment and disinfection. J Mol Liq 303:112640

Nodeh HR, Kamboh MA, Ibrahim WAW et al (2019) Equilibrium, kinetic and thermodynamic study of pesticides removal from water using novel glucamine-calix[4]arene functionalized magnetic graphene oxide. Environ Sci Process Impacts 21:714–726

Notriawan D, Angasa E, Suharto TE et al (2013) Green synthesis of silver nanoparticles using aqueous rinds extract of Brucea javanica (L.) Merr at ambient temperature. Mater Lett 97:181–183

Ofomaja AE (2010) Intraparticle diffusion process for lead(II) biosorption onto mansonia wood sawdust. Bioresour Technol 101:5868–5876

Parlayıcı, Pehlivan E (2017) Removal of metals by Fe3O4 loaded activated carbon prepared from plum stone (Prunus nigra): kinetics and modelling study. Powder Technol 317:23–30. https://doi.org/10.1016/j.powtec.2017.04.021

Patel H (2020) Batch and continuous fixed bed adsorption of heavy metals removal using activated charcoal from neem (Azadirachta indica) leaf powder. Sci Rep 10:1–12

Pholosi A, Naidoo EB, Ofomaja AE (2020) Intraparticle diffusion of Cr(VI) through biomass and magnetite coated biomass: a comparative kinetic and diffusion study. South African J Chem Eng J 32:39–55. https://doi.org/10.1016/j.sajce.2020.01.005

Thilakan D, Patankar J, Khadtare S, et al (2022) Plant-derived iron nanoparticles for removal of heavy metals. Int J Chem Eng 2022. https://doi.org/10.1155/2022/1517849

Torab-Mostaedi M, Asadollahzadeh M, Hemmati A, Khosravi A (2013) Equilibrium, kinetic, and thermodynamic studies for biosorption of cadmium and nickel on grapefruit peel. J Taiwan Inst Chem Eng 44:295–302

Truong TTV, Chen C-C, Kumar SR et al (2022) Prismatic silver nanoparticles decorated on graphene oxide sheets for superior antibacterial activity. Pharmaceutics 14:924

Uçar D, Armağan B (2012) The removal of reactive black 5 from aqueous solutions by cotton seed shell. Water Environ Res 84:323–327

Wang T, Zheng L, Liu Y et al (2020) A novel ternary magnetic Fe_3O_4/g-C_3N_4/Carbon layer composite for efficient removal of Cr (VI): a combined approach using both batch experiments and theoretical calculation. Sci Total Environ 730:138928

Wang Q, Wang Y, Yang Z et al (2022) Efficient removal of Pb(II) and Cd(II) from aqueous solutions by mango seed biosorbent. Chem Eng J Adv 11:100295. https://doi.org/10.1016/j.ceja.2022.100295

Wong KT, Eu NC, Ibrahim S et al (2016) Recyclable magnetite-loaded palm shell-waste based activated carbon for the effective removal of methylene blue from aqueous solution. J Clean Prod 115:337–342. https://doi.org/10.1016/j.jclepro.2015.12.063

Yu JX, Wang LY, Chi RA et al (2013) Competitive adsorption of Pb^{2+} and Cd^{2+} on magnetic modified sugarcane bagasse prepared by two simple steps. Appl Surf Sci 268:163–170. https://doi.org/10.1016/j.apsusc.2012.12.047

Yuliusman, Nasruddin, Afdhol MK et al (2017) Preparation of activated carbon from palm shells using KOH and $ZnCl_2$ as the activating agent. IOP Conf Ser Earth Environ Sci 75:012009. https://doi.org/10.1088/1755-1315/75/1/012009

Zaini MAA, Okayama R, Machida M (2009) Adsorption of aqueous metal ions on cattle-manure-compost based activated carbons. J Hazard Mater 170:1119–1124

Zhang W, Ding L, Luo J et al (2016) Membrane fouling in photocatalytic membrane reactors (PMRs) for water and wastewater treatment: a critical review. Chem Eng J 302:446–458

Zhang S, Wang Z, Chen H et al (2018) Polyethylenimine functionalized Fe_3O_4/steam-exploded rice straw composite as an efficient adsorbent for Cr (VI) removal. Appl Surf Sci 440:1277–1285

Zhou N, Chen H, Feng Q et al (2017) Effect of phosphoric acid on the surface properties and Pb (II) adsorption mechanisms of hydrochars prepared from fresh banana peels. J Clean Prod 165:221–230